



This is a repository copy of *Micromechanical testing and microstructure analysis of as-welded and post-weld heat-treated Ti-6Al-4V alloy*.

White Rose Research Online URL for this paper:

<https://eprints.whiterose.ac.uk/219515/>

Version: Published Version

Article:

Lu, Y., Turner, R. orcid.org/0000-0003-1751-0448, Fang, C. et al. (4 more authors) (2024) Micromechanical testing and microstructure analysis of as-welded and post-weld heat-treated Ti-6Al-4V alloy. *Journal of Materials Science*, 59. pp. 19960-19976. ISSN 0022-2461

<https://doi.org/10.1007/s10853-024-10348-6>

Reuse

This article is distributed under the terms of the Creative Commons Attribution (CC BY) licence. This licence allows you to distribute, remix, tweak, and build upon the work, even commercially, as long as you credit the authors for the original work. More information and the full terms of the licence here:

<https://creativecommons.org/licenses/>

Takedown

If you consider content in White Rose Research Online to be in breach of UK law, please notify us by emailing eprints@whiterose.ac.uk including the URL of the record and the reason for the withdrawal request.



eprints@whiterose.ac.uk
<https://eprints.whiterose.ac.uk/>



Micromechanical testing and microstructure analysis of as-welded and post-weld heat-treated Ti-6Al-4V alloy

Yu Lu^{1,*}, Richard Turner^{1,*} , Chizhou Fang², Feng Wang¹, Jeffery Brooks¹, Biao Cai¹, and Hector Basoalto²

¹ School of Metallurgy and Materials, University of Birmingham, Birmingham B15 2TT, United Kingdom

² Department of Materials Science and Engineering, University of Sheffield, Mappin Street, Sheffield S1 3JD, UK

Received: 30 July 2024

Accepted: 15 October 2024

Published online:

1 November 2024

© The Author(s), 2024

ABSTRACT

The microstructural evolutions and variations in mechanical performance of electron beam welded (EBW) Ti-6Al-4V (Ti64) alloy have been investigated. The effects of heat treatment on the microstructure of welded samples have been studied after post-welding solution treatment and ageing. The martensitic phase α' has been confirmed using transmission electron microscopy (TEM). Electron backscatter diffraction (EBSD) has been used to investigate the phase and grain morphology. Results showed that the martensitic α' phase coarsened, the size of heat-affected zone (HAZ) changed and grains in the base materials (BMs) had grown after the post-weld heat treatments (PWHT). The tensile behaviour of electron beam welded Ti64 has been investigated using in situ tensile testing monitored by optical microscopy. The deformation and failure were directly revealed during the in situ tensile process. Results showed that the EBW Ti64 samples have different failure locations after receiving different post-weld heat treatments. The relationship between the post-weld heat treatments, microstructural evolution and mechanical properties of EBW Ti64 were investigated. Thermodynamic databases were used to predict mechanical properties—including the yield strengths—of the titanium alloy for different grain sizes, representing different post-weld heat treatment operations, and these were embedded into a finite element modelling framework to simulate the tensile testing specimens to understand the mechanical fields experienced such as stresses and strains, just prior to failure.

Handling Editor: Megumi Kawasaki.

Address correspondence to E-mail: y.lu.2@bham.ac.uk; r.p.turner@bham.ac.uk

Introduction

The low density, good fatigue property, excellent strength-to-density ratio and high corrosion resistance of titanium (Ti) alloys have attracted numerous industries to explore their wide range of application for demanding performance and reliability requirements. These industries include aerospace, automotive, nuclear and power generation industries [1–3]. To meet the fabrication requirement of larger and more complex components, various welding techniques have been developed for use with Ti alloys, such as gas tungsten arc welding (GTAW), plasma arc welding (PAW), laser beam welding (LBW) and electron beam welding (EBW). Electron beam welding, in particular, is highly effective for titanium alloys due to the entire welding process being conducted in a high vacuum environment, which protects the hot metal from gaseous contamination [4]. Furthermore, EBW can produce a narrower, deeper molten pool due to the high energy density of the heat source [5, 6], which is advantageous for minimising component distortions, although careful control of processing parameters is required to manage the formation of a keyhole-containing vapour phase of the alloy.

The strength and ductility of welded titanium alloys can be significantly affected by their thermal history. Post-weld heat treatments (PWHTs) are commonly applied after welding to relieve residual stresses, modify the microstructure and therefore alter the mechanical properties. The literatures reported that PWHT has significant influence on the resulting microstructure of welds, which in turn greatly affects the mechanical properties of processed titanium alloys [7–10]. TC17 alloys processed using EBW and subjected to PWHT conducted at 630°C for 2h have shown improved mechanical properties, with an ultimate tensile strength σ_{UTS} of 1138 MPa and elongation of 10.27% [11]. Tsai et al. reported that a Ti64 alloy, after an annealing treatment (790°C/1h/argon-cooled {AC}), achieved a yield strength of 1084 MPa and elongation of 9.7% [12]. Ti-15-3 welds exhibited a tensile strength of 1257 MPa and elongation of 10% because of the precipitation of nanosized α phase after ageing (538°C/8h/AC) [13]. It has been reported that the tensile strength is the highest in the as-welded condition and lowest in the solution-treated and aged (STA) condition of Ti64 [8].

Away from base material properties, Hayes et al [14] reported upon tensile property measurements

for Ti64 alloy manufactured via direct laser deposition (DLD), to understand the variation from base properties that a microstructure typical to this highly rapid deposition and cooling process may offer. They modelled the behaviour using equations to account for strengthening mechanisms including Taylor hardening and Hall–Petch strengthening via both α laths and colonies. Micromechanical testing of Ti64 produced via laser powder bed fusion (LPBF) manufacturing was studied by Mishurova et al [15] by synchrotron X-ray diffraction tensile methods. Distinct variation in radial and axial direction behaviour was observed, due to metallurgical effects including compression twinning, and accumulation of intergranular strains.

Finite element modelling methods have been employed to further the understanding of the thermo-mechanical behaviour of Ti64 under different manufactured conditions. Yang et al [16] predicted thermal fields, and arising stress distributions during the DLD additive processing route for Ti64, while Ding et al [17] performed thermomechanical analyses for both wire and arc additive layer manufacture (WAALM) to again understand thermal cycles and the associated emerging stress fields. For multi-pass welded Ti64, Chiumenti et al [18] used quiet element and born-dead element methods to predict distortion, stress development and metallurgical features such as hot-cracking phenomena within different geometries. Lu et al [19] using FE to predict the thermal fields induced within the alloy and energy deposition rates during an electron beam welding operation upon Ti64 plate. Joun et al [20] developed an FE framework to computationally perform a digital twin tensile test, primarily to consider the necking phenomenon within the gauge length, using commercial forging simulator tool AFDEX2D. While this was not performed for the Ti64 alloy of interest, it offers guidance regarding FE model set-up, with relevant materials properties for the Ti64 alloy able to be dropped in to place. However, limited studies have been focused on the combination of experimental characterisation, numerical prediction of microstructure and mechanical fields, such as stresses during in situ tensile testing of Ti64 welds.

In this study, Ti64 samples were fabricated using electron beam welding at different energy densities and subjected to various thermal histories. The influence of these post-weld heat treatments on the microstructure and mechanical properties were investigated through in situ tensile testing while observing the samples under an optical microscope. Moreover, a

numerical model was employed to study the variation in the mechanical fields of stress and strain within the welded joints caused by the PWHT during the tensile testing process.

Experimental and methods

Materials and preparation

Ti-6Al-4V alloy plates, with a thickness of 1 mm, were welded at Bodycote using the autogenous bead-on-plate electron beam welding method. The chemical composition (wt.%) of the Ti-6Al-4V alloy is as follows: Al-6.24, V-3.96, C-0.018, Fe-0.003, O-0.072, N-0.007, H-0.0025 and Ti-balance. All the plates were welded at a constant beam voltage of 140kV and beam current of 3mA, using two different speeds of 15 mm/s and 42 mm/s. The descriptive parameter 'energy per unit length' was used to quantify the energy density, given in Equation 1.

$$\text{Energy per unit length (J/mm)} = \frac{\text{Voltage} \times \text{Current}}{\text{Travel Speed}} \quad (1)$$

Post-weld heat treatments were then carried out. The ageing treatment (A) was performed at 790°C for 1h, followed by argon cooling. The solution-treated and aged (STA) samples were solution treated at 950°C for 1h, followed by fast quenching (FQ), and then aged at 790°C for 1h followed by argon cooling. These heat treatments were conducted in a furnace with high-purity argon atmosphere, and the heating rate was 20°C/min. STA is performed industrially to improve mechanical properties on bulk Ti-6Al-4V; however, it was of interest to understand if the small volume of material in a weld bead, with the significantly different initial microstructure, demonstrated

similar mechanical gains. The conditions of as-welded and post-weld heat-treated samples are shown in Table 1.

The metallography specimens were sectioned transversely to the welding direction and polished down to 0.04 µm. The samples were then etched in a solution containing 2 ml HF, 10 ml HNO₃ and 88 ml H₂O. For EBSD investigation, electropolishing was carried out in a solution of 10% perchloric acid and 90% methanol at 10°C, using 10 Volts for 20s.

Microstructural characterisation

A Zeiss Axioskop 2 microscope equipped with Axio-Vision image capture and analysis software was employed to observe the macroscopic structure. Grain size analysis was performed using Image J software and planimetric method according to the American Society (ASTM) E112-12 standards, with errors reported as standard deviations less than ±25µm. A JEOL JSM-7000F scanning electron microscope (SEM) was used for microstructure observation and electron backscatter detection (EBSD) analysis. Aztec software was used for acquiring crystal orientation data and post-processing analysis. Suitable magnification was selected to observe an adequate number of grains for better statistical estimation. An FEI Quanta 3D field emission gun (FEG) focused ion beam (FIB) SEM was employed to prepare the sample from the fusion zone. Identification of martensitic phases was carried out using a Tecnai F30 transmission electron microscope (TEM). The different weld zones were distinguished based on microstructural differences observed. The locations of the weld pool dimensional measurements are described in Figure 1.

Table 1 Experimental matrix for the fusion (EB) welding trials.

Sample No.	Condition	Current (mA)	Voltage (kV)	Travel speed (mm/s)	Energy per unit length (J/mm)
1	EBW	3	140	15	28
2	EBW	3	140	42	10
A1	EBW +790°C/1h/AC	3	140	15	28
A2	EBW+790°C/1h/AC	3	140	42	10
STA1	EBW +950°C/1h/FQ+790°C/1h/AC	3	140	15	28
STA2	EBW +950°C/1h/FQ+790°C/1h/AC	3	140	42	10

FQ: fast quenching (100°C/min); AC: argon cooling (40°C/min)

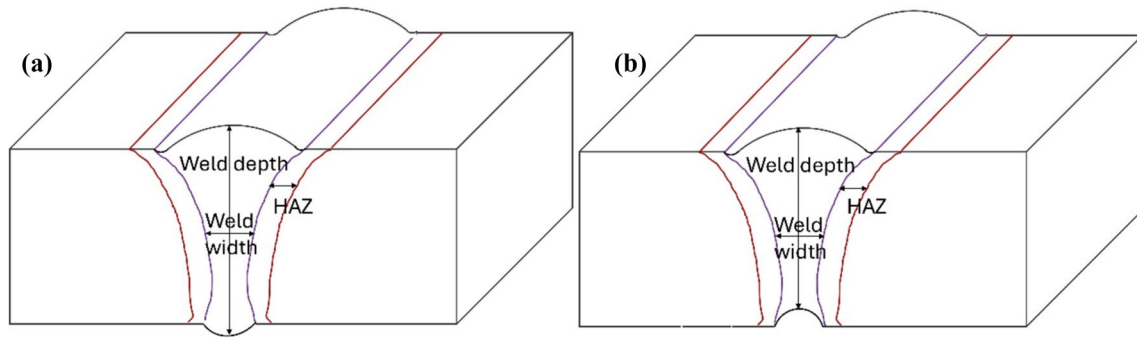


Figure 1 Schematic drawings showing the dimensional measurements of the weld pool: **a** the weld conducted at 28 J/mm energy density; **b** the weld conducted at 10 J/mm energy density.

In situ tensile test

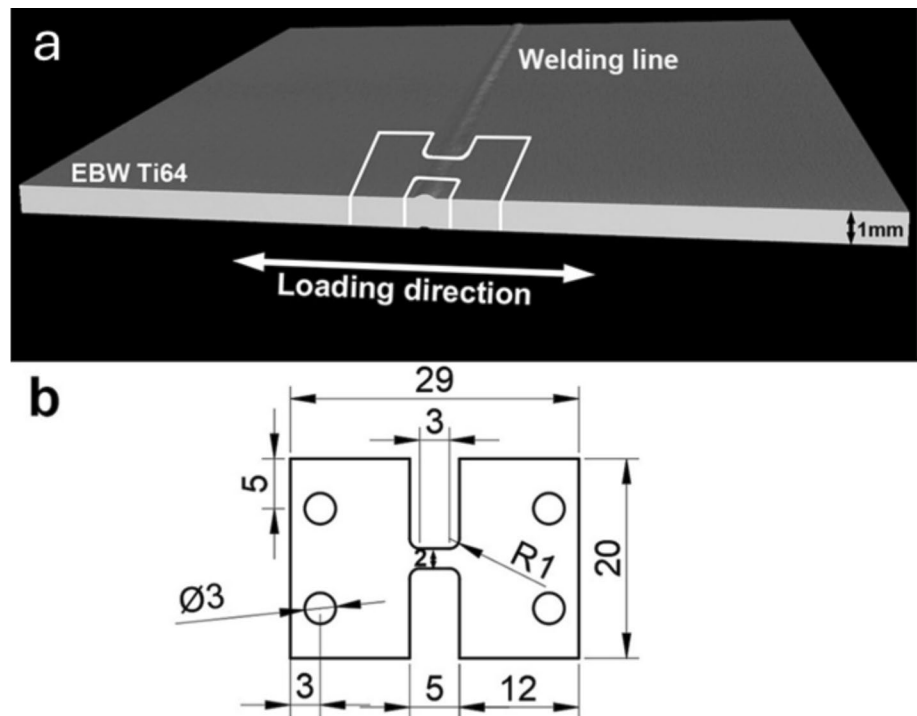
Figure 2 schematically shows the sampling method and the dimensions of the tensile specimens. In situ tensile testing was carried out on an optical microscope (Zeiss Stemi 508) at a tensile speed of 0.2 mm/min on a Deben MT5000 micromechanical testing machine accessory with a maximum load capacity of 2000N. Optical images of the specimen were collected using Zeiss ZEN core software during the tensile testing to evaluate stress-strain behaviour at

room temperature. The morphology of the fracture surface of the sample was then observed using SEM.

Three-dimensional modelling framework

A finite element (FE) model of the tensile testing sample during tensile loading was prepared, to allow a greater understanding of the stress distribution within the sample during tensile loading and close to failure. As such, the 3-dimensional (3D) tensile test-piece geometry was recreated within the

Figure 2 **a** Schematic illustration of the sampling method; **b** geometry of the tensile sample (in mm)



general metal-forming FE software Deform (v12.0). The 2-dimensional (2D) outline was recreated as a series of Cartesian coordinates, and meshed as a 2D part, and the geometry was then swept through in to 3D using the software inbuilt features. As such, the element type used was a 3D brick hexahedral element (see Figure 3). The workpiece was sectioned into three different regions, regions one and three comprising of the grips, and consisting of parent Ti-6Al-4V material, and region two representing the weld zone material, located at the centre of the gauge length of the specimen, containing both the weld bead, and the very narrow band of heat-affected zone (HAZ) material either side of the bead. For simplicity, and to allow the software 2D to 3D sweep functionality to work, the weld zone was represented as a simple straight edged section, without any tapering through the thickness. A mesh size of between 0.9 mm element edge length (coarse regions) and 0.09 mm element edge length (fine regions) was employed, with a time-step of 0.005 s.

A simplified planar clamping arrangement, representative of the tensile testing machine with the workpiece unable to detach from the machine at the interface was implemented. The tensile tester grips were moved at a representative speed, and the load required for this deformation was then calculated by the FE software.

The thermodynamic materials properties database JMatPro (version 10.1) was consulted to generate predictions of the bulk thermomechanical properties of

the Ti-6Al-4V alloy in the different weld regions, with the different heat treatment operations [21, 22]. These bulk materials properties, as calculated in the JMatPro software for the composition and mean grain size measured, are presented in the results.

Results

Metallography

EBW Ti64 welds with transitional microstructures are presented in Figure 4. The welds were obtained using the different welding parameters and post-weld heat treatments (PWHTs). No volumetric defects were detected. The microstructure of the EBW welds can be divided into three zones: fusion zone (FZ), heat-affected zone (HAZ) and base material (BM). The FZ and HAZ were clearly distinguished from the BM because of their significantly different microstructures.

All of the welds were fully penetrated, but with different weld pool geometries across the two different weld energy density. The welds with larger energy density (28J/mm) have larger weld width and depth (Table 2). As the weld pool geometry itself is frozen once the weld has cooled, so clearly no variation in pool geometry can be observed for different PWHT conditions. However for repeatability, the weld pool geometry for each weld density and PWHT condition was re-measured for completeness. The HAZ became smaller compared with the as-welded samples. The

Figure 3 a 2D outline of sectioned regions within the tensile specimen, b the 3D meshed tensile specimen and c shown from isometric view for the sample depth.

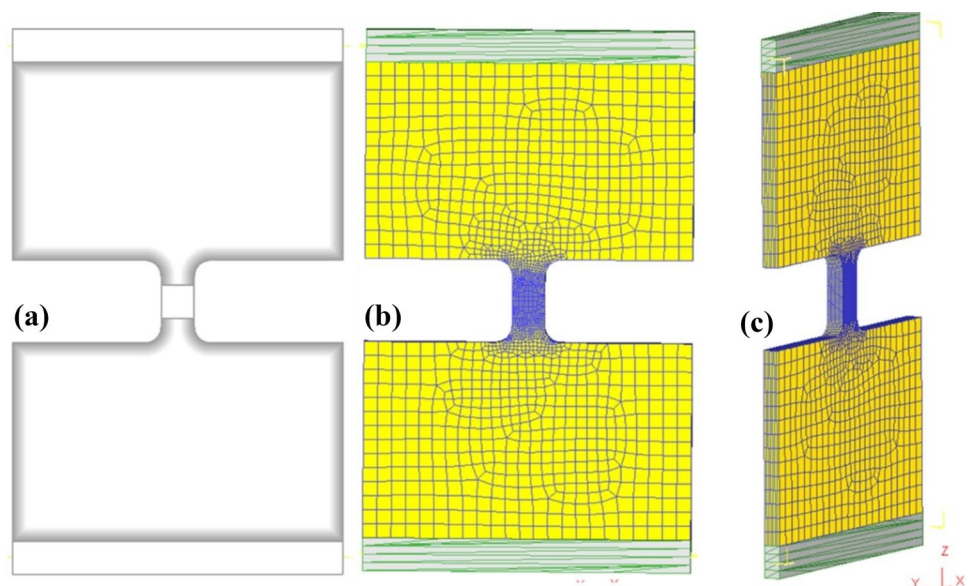


Figure 4 Cross-sectional metallographic characterisation of EBW Ti64 welds: **a** Sample 1, 28J/mm (as-welded); **b** Sample 2, 10J/mm (as-welded); **c** Sample A1, 28J/mm (post-aged); **d** Sample A2, 10J/mm (post-aged); **e** Sample STA1, 28J/mm (post-ST-aged); **f** Sample STA2, 10J/mm (post-ST-aged).

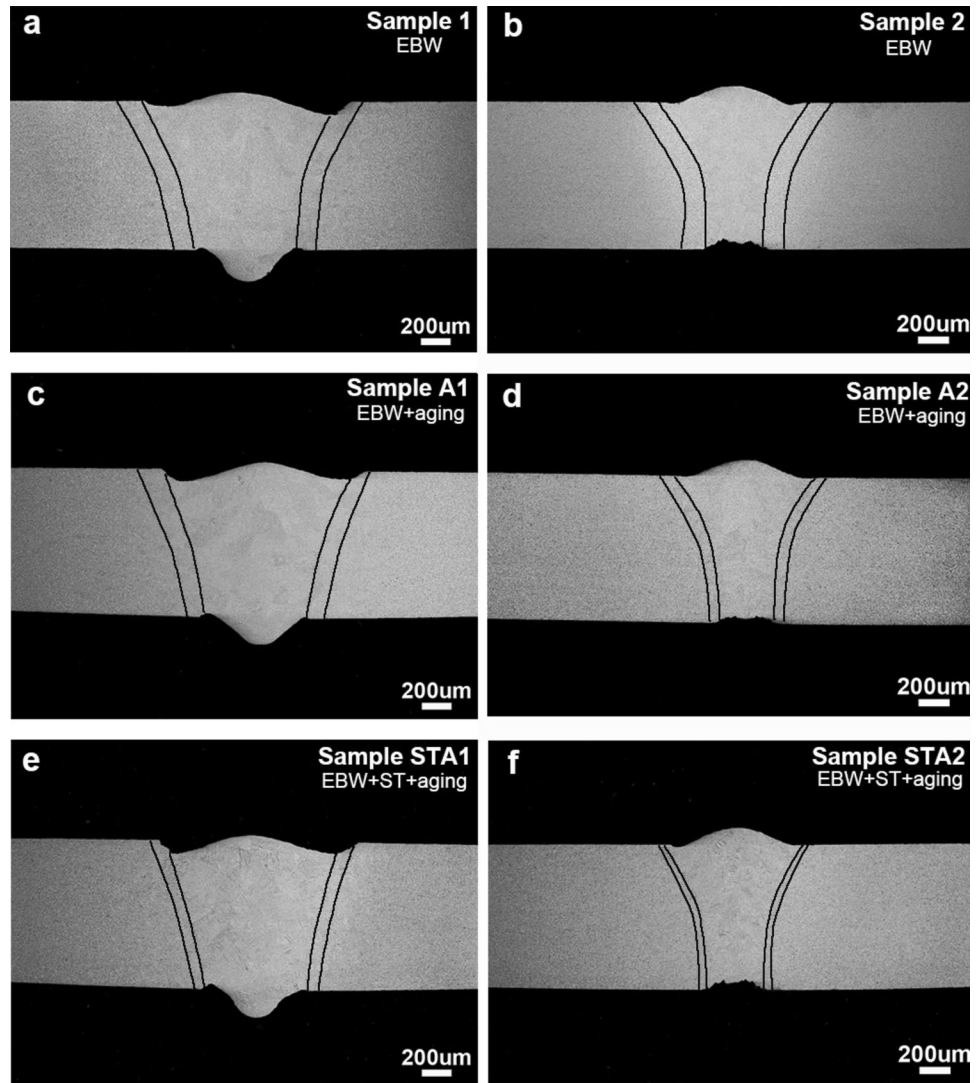


Table 2 Weld geometry and grain size (GS) of EBW Ti64 samples.

	Weld Geometry			GS in FZ (µm)
	Depth (mm)	Width (mm)	HAZ (mm)	
Sample 1	1.24	0.83	0.15	120
Sample 2	1.06	0.47	0.13	95
Sample A1	1.23	0.83	0.11	180
Sample A2	1.07	0.46	0.08	142
Sample STA1	1.23	0.82	0.07	228
Sample STA2	1.05	0.45	0.05	177

narrowest width of HAZ was observed in solution-treated aged (STA) samples STA1 and STA2. The larger energy density welds have a larger grain size (GS), in

both as-welded and PWHT conditions (Table 2). The grain size in the fusion zone (FZ) was greatly increased after the STA treatment, from 120 µm to 228 µm on Sample 1 and from 95 µm to 177 µm on Sample 2, respectively.

α-β microstructure evolution in different locations of welds

SEM images show that the microstructure significantly changed from the FZ to the BM through HAZ of EBW Ti64 welds (Figure 5). In the as-welded samples, the microstructure of FZ was as-solidified coarse β columnar grain structure and consisted of fine martensitic α' needles with a length of over 15 µm (Figure 5 (a) and (d)). As shown in Figure 5 (b) and (e), the HAZ of as-welded samples showed a phase transformation

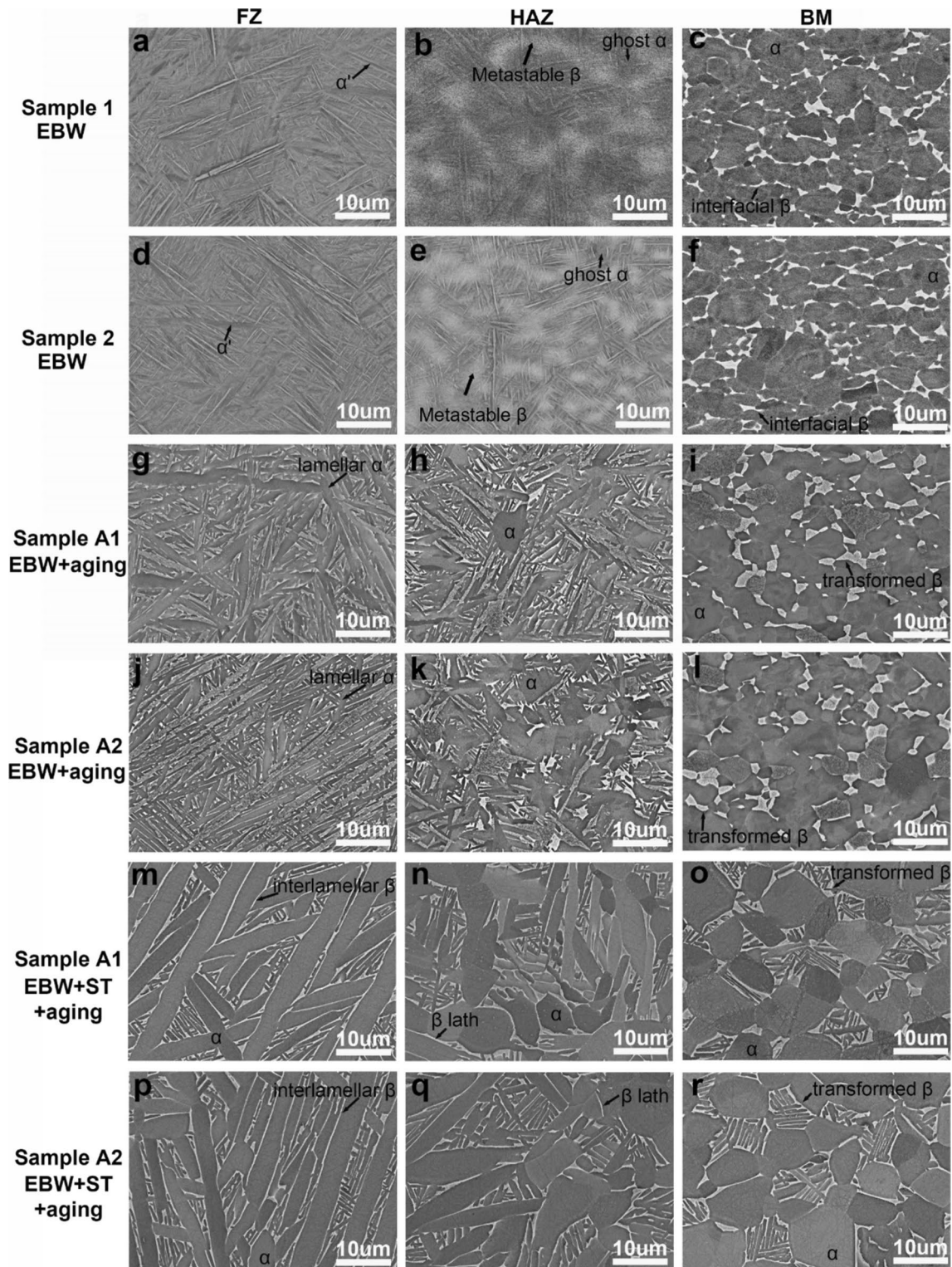


Figure 5 SEM images of different zones: **a-c** Sample 1, 28J/mm (as-welded); **d-f** Sample 2, 10J/mm (as-welded); **g-i** Sample A1, 28J/mm (post-aged); **(j-l)** Sample A2, 10J/mm (post-aged); **m-o**

Sample STA1, 28J/mm (post-ST-aged); **p-r** Sample STA2, 10J/mm (post-ST-aged).

phenomenon which contains fine α in metastable β phases. Due to the fast-cooling rate during the welding process, there is insufficient time for transforming from β phase to the equilibrium α phase in the HAZ [23]. The BM of as-welded samples contain mainly α with some dispersed interfacial β , as shown in Figure 5 (c) and (f). The significant coarsening of martensitic α' phase in the FZ can be observed in both 10 J/mm and 28 J/mm samples after PWHT. The FZ structure was transformed to a platelet α with interlamellar β in the STA conditions compared with the martensite in the as-welded conditions. When the welds were heat treated at 950°C, the diffusion coefficients of alloying elements improved, therefore the ghost α phases decomposed into α and β phase laths in the HAZ. The post-weld aged samples have more equiaxed interfacial β in the BM. The microstructure of the BM after PWHT was bimodal and consisted of primary α and a transformed structure of β phases (Figure 5 (i), (l), (o) and (r)).

Typical TEM micrographs of the FZ of EBW Ti64 are shown in Figure 6. The large number of acicular phases (α') can be observed. The selected area diffractions (SADs) obtained from framed area was identified as martensitic phase α' (Hexagonal, $a=2.95\text{\AA}$, $c=4.68\text{\AA}$). The martensitic phase α' of Sample 1 is finer than that of Sample 2.

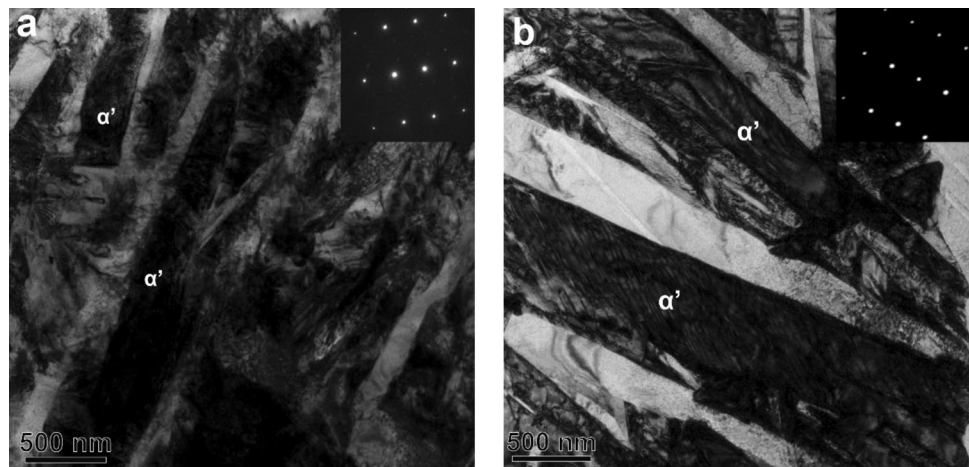
Figure 7 presents the inverse pole figure (IPF) maps and $\{0001\}_\alpha$ pole figures of the EBW Ti64 samples. It can be seen that fine martensitic α' needles appeared in the FZ of as-welded samples (Figure 7 (a) and (e)). In both welds considered in this work, the general columnar nature of the grains in the FZ can be observed. The moderate heat energy per unit length inputs has been

performed in these electron beam welding operations; one would assume that this will induce higher thermal gradients, which lend to columnar grain formation more readily. For the heat energy, 28 J/mm is approximately triple compared with 10 J/mm, which indicates that more heat input was transferred into the material per unit time. The higher heat input in the Sample 1 has kept the material in the FZ above the β transus longer which has allowed grain growth to occur which has reduced the columnar nature of the grains. Thus, the grain morphology appears relatively less columnar and grain size is larger. Compared with the as-welded samples, the FZ in the heated-treated samples show the similar components but different intensity (Figure 7 (l), (p), (t) and (x)). In the BM maps of as-welded samples (Figure 7 (c) and (g)), the majority of grains appear to be fine and uniform. Most of the BM structures correspond to deformed grains elongated along the similar direction, with grain c -axes parallel to the normal direction (ND) of the surface (Figure 7 (d) and (h)). After the PWHT, the BM has a lower α -texture intensity. For the PWHT samples, IPF figures (Figure 7 (k), (o), (s) and (w)) show that the well-defined equiaxed grains in the BM were considerably increased along with the occurrence of coarsening. The microstructure of the FZ reveals large β grains containing lamella structure. The significant coarsening of martensitic phase and grain size occurred after the PWHT.

In situ tensile test

Table 3 illustrates the tensile properties of EBW Ti64 samples measured by in situ tensile testing. EBW samples have larger ultimate tensile strength (σ_{UTS}), yield

Figure 6 Bright field images and selected area electron diffraction patterns taken along $\langle 1\bar{1}00 \rangle$: **a** Sample 1 and **b** Sample 2, showing typical martensitic phase α' .



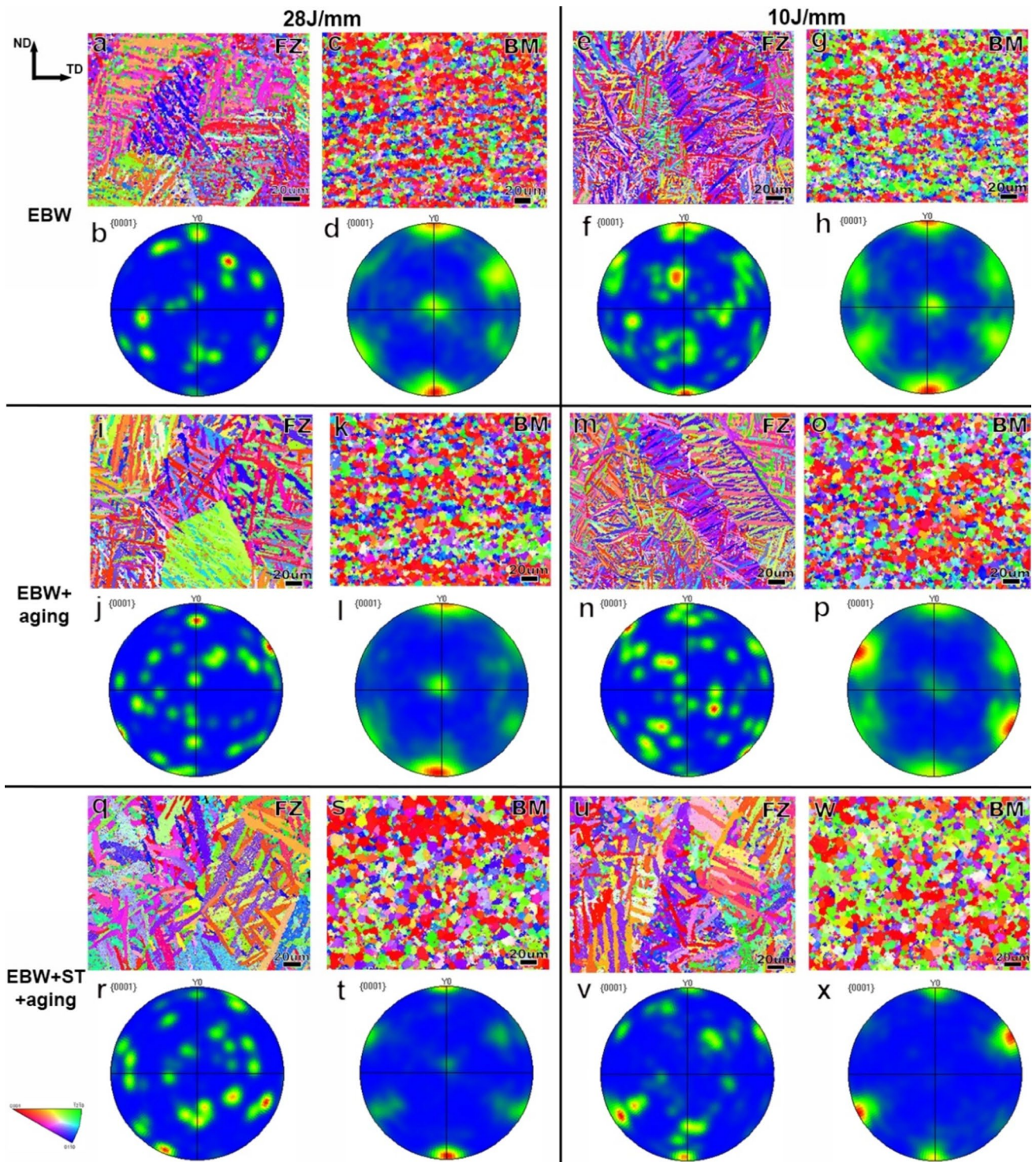


Figure 7 Inverse pole figure maps and $\{0001\}$ pole figures of EBW Ti64 samples after different heat treatments, which obtained from FZ and BM: **a-d** Sample 1, 28J/mm (as-welded); **e-h** Sample 2, 10J/mm (as-welded); **i-l** Sample A1, 28J/mm

(post-aged); **m-p** Sample A2, 10J/mm (post-aged); **q-t** Sample STA1, 28J/mm (post-ST-aged); **u-x** Sample STA2, 10J/mm (post-ST-aged).

Table 3 Mechanical properties of EBW Ti64 welds in various conditions.

Sample No.	Conditions	Tensile Properties (including +/- standard deviations)		
		σ_{UTS} (MPa)	σ_{YS} (MPa)	% E
1	EBW	1206±8	1080±12	19.1±1.6
2	EBW	1152±3	993±7	24.2±2.0
A1	EBW +790°C/1h/AC	1193±9	1054±7	17.7±0.7
A2	EBW+790°C/1h/AC	1133±6	987±11	22.1±0.9
STA1	EBW+950°C/1h/FQ+790°C/1h/AC	1158±10	1043±8	16.3±0.7
STA2	EBW+950°C/1h/FQ+790°C/1h/AC	1107±8	954±5	20.7±0.6

strength (σ_{YS}) and elongation (%E) compared with the parent Ti64 (σ_{UTS} : 927±11 MPa; σ_{YS} : 843±10 MPa; %E: 11.5±1.9%), which means that the EBW process can significantly improve the joint efficiency of Ti64. The excellent tensile strength and ductility can be found in the as-welded samples compared with that of PWHT samples. The fracture occurs in the BM of as-welded samples which indicates that the welded joint exhibits higher strength than BM. The high ductility of the as-welded samples is due to the fine acicular α' . For the STA samples, the tensile strength further decreases as compared with the as-welded and aged samples, and the fracture happens at the FZ. The coarse grain size and martensitic phase provide detrimental influences on the joint efficiency. Thus, the microstructures in the welded region can significantly affect the mechanical properties of welds.

The observations of EBW Ti64 welds during the in situ tensile tests are shown in Figure 8. With increasing strain, samples are shown under elastic deformation, at yield, during necking and at failure. The necking within the sample gauge length can be clearly observed. The cracks originated from the surface of the tensile samples. The fracture of the as-welded samples took place in the BM region of the gauge length, indicating the high strength of the joint compared with the BM. For the post-weld aged welds, the crack initiates at the side of HAZ/BM and then propagates along the interface. However, the crack in the STA welds initiated in the FZ.

One anomaly that seemingly is presented when considering the results from tensile experiments is that for the as-welded Samples 1 and 2, the fracture occurs in the base material (i.e. outside of the weld bead) yet the tensile strength derived from these experiments is considerably higher than that of the parent Ti64. It was hypothesised that this seeming anomaly in the results

has arisen due to the small gauge length in the small tensile specimen, further constrained by the stronger weld bead in the centre of the gauge length, causing a stress concentration effect. To attempt to rationalise this, FE modelling was consulted. By interrogating the FE model, the inputted stress-strain data for the parent material was compared to the predicted σ_z (tensile direction) stress and strain values extracted from nodes in the location that the real experiment fractured, for all of the tensile test-piece simulations. It was noted that the arising stress-strain behaviour predicted at the critical location in the gauge length was higher than the inputted material stress-strain curve data.

When consulting the experiment different fracture morphology and locations from different conditions of EBW Ti64 samples are evident. A stronger weld bead which is present within the gauge length can act as a stress concentrator. As-welded samples failed outside of the weld zone, and therefore tensile test measured the parent Ti64 material. The as-welded samples were most significantly affected by stress concentrator issues from the stronger weld bead adjacent to HAZ and to parent Ti64 material, as the thermal gradients in these welds were so sharp, and with no subsequent heat treatment operation to attempt to reduce the sharp transitions of fine martensitic needles and much refined grains in the weld, to the considerably larger grains of the parent Ti64.

Thermodynamic predictions of mechanical properties

The bulk mechanical properties for the parent zone and the fusion/weld bead zone were calculated, for use within the FE computation, using the thermodynamic database JMatPro, by Sente Software. The

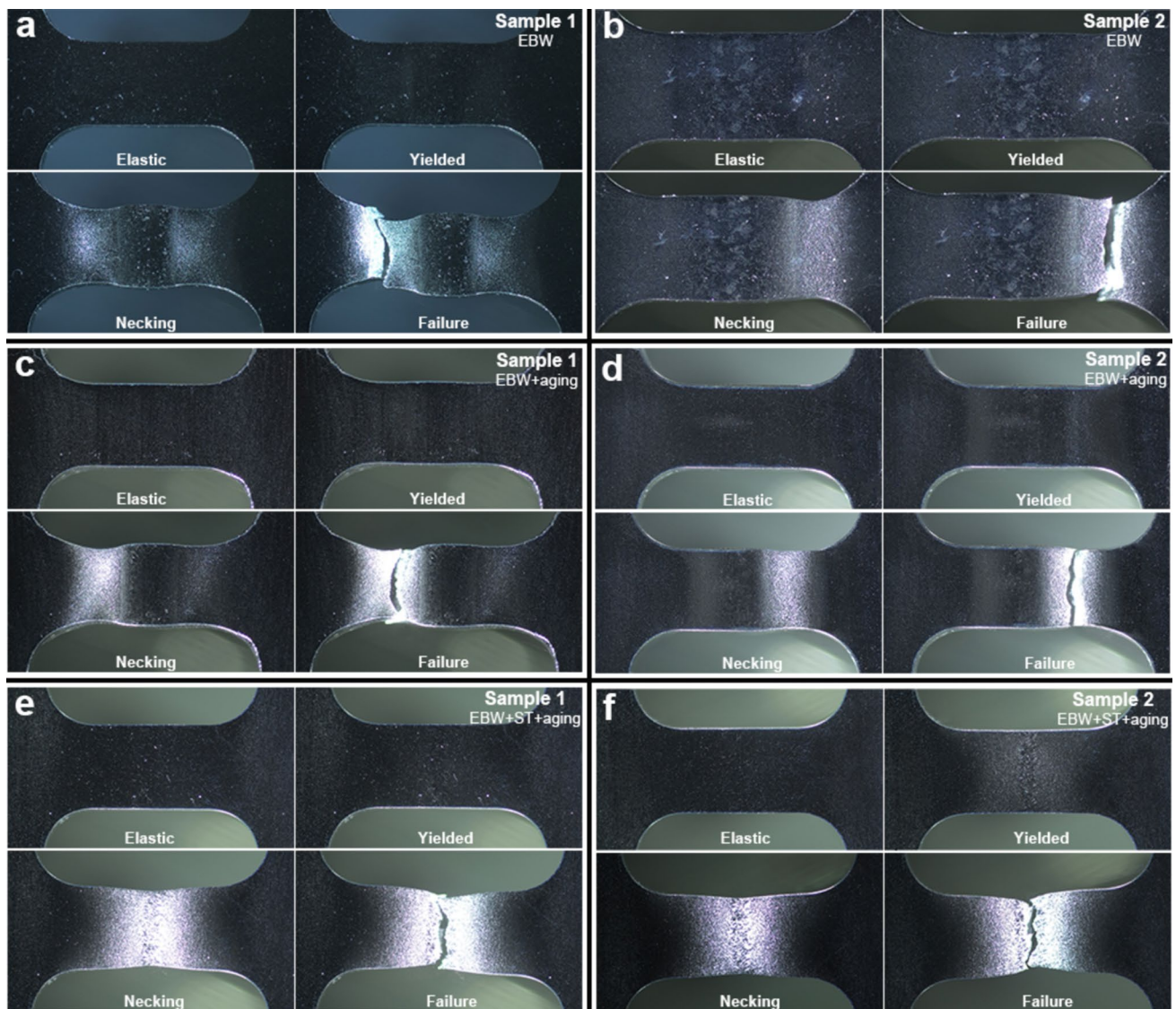


Figure 8 Selected optical images of EBW Ti64 welds during in situ tensile tests: **a** Sample 1, 28J/mm (as-welded); **b** Sample 2, 10J/mm (as-welded); **c** Sample A1, 28J/mm (post-aged); **d**

Sample A2, 10J/mm (post-aged); **e** Sample STA1, 28J/mm (post-ST-aged); **f** Sample STA2, 10J/mm (post-ST-aged).

mechanical properties of the processed titanium alloy are strongly dependent upon the precise variations in microstructural details caused by the heat treatment operations, including characteristics such as elongation of β phase and texture development in α . However, to compute a set of simplified, isotropic material properties, which could be inputted into an isotropic FE simulation, the measured chemical composition of the alloy, the heat treatment temperature specified for each condition and an approximate mean grain size of the weld bead material, was required.

Predictions for the stress-strain curves are presented in Figure 9. The thermodynamic software is predicting the elastic yield limit to be approximately 970 MPa for the Samples 1 and 2, and marginally lower, at 950–960 MPa for the ageing heat-treated Sample A1 and A2, whereas it is predicting the elastic yield to occur at approximately 925 MPa for the solution-treated STA1 and STA2 conditions (Figure 9).

When compared with the measured tensile yield data, it becomes clear that the JMatPro software is performing reasonably well in the prediction of the Sample 2, Sample A2 and Sample STA2, with a small

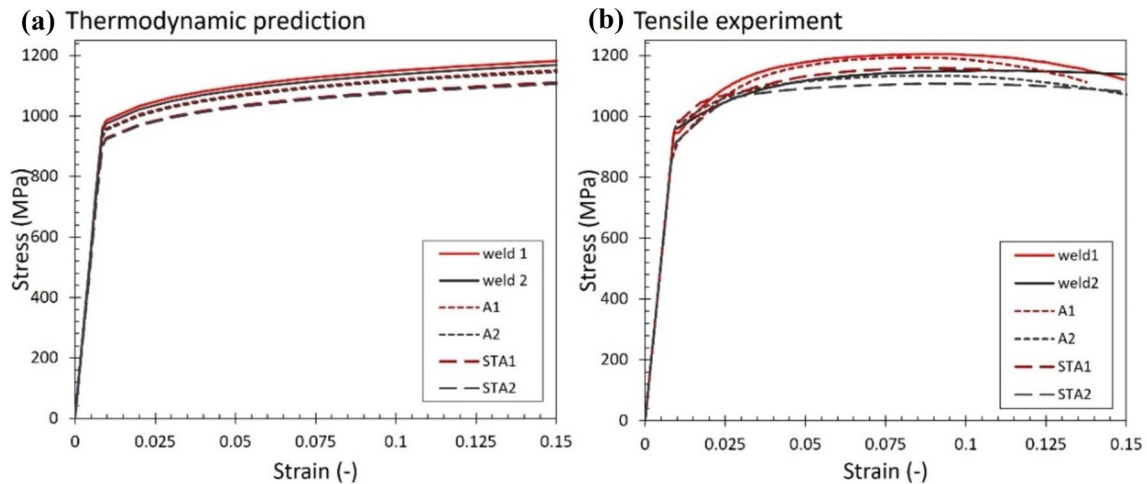


Figure 9 Predicted stress-strain curves (at room temperature and 10^{-3} s^{-1} rate) for the different weld zones, in differing heat treat conditions, from; **a** JMatPro software predictions, **b** tensile experiment.

under-prediction of 2 to 3% in the predicted tensile yield strength. However, the predictions perform less well for the Sample 1, and the subsequent treatments experienced by weld bead 1, with under-predictions of approximately 10% for each yield strength prediction, particularly the as-welded and the aged conditions for weld 1.

The full stress-strain curves generated from the experimental data and the thermodynamic predictions do illustrate that the software was predicting only very small variations for the two different weld specimens, with the heat treatment conditions having a larger impact on the material behaviour, whereas the experimental data indicated the reverse trend, that the two different welds were the primary cause of the stress-strain difference, with the heat treatment effects of secondary importance. It is hypothesised therefore that the grain sizes and microstructure emerging from the EB welding process of weld 1 has differed to those from weld 2, due to significantly different cooling rates, which was not able to be accurately captured within the inputs used for the thermodynamic modelling.

Mechanical fields during tensile testing

Finite element (FE) modelling using the commercial FE code Deform (v12.0) was created to understand arising mechanical fields during tensile loading of the specimens, with material properties as predicted by JMatPro thermodynamic software coded into

different regions of the geometry, to represent parent and weld bead material. As such, the model was interrogated to determine the associated stress (Figure 10 (a)) and strain (Figure 10 (b)) fields in the tensile loading (Z) axis, and any associated likelihood for cracking to occur, using the normalised Cockroft and Latham damage parameter.

Given the considerable similarity between the stress-strain curves for the as-welded bead and the heat-treated weld bead, these models were very similar. The predictions for the damage parameter for the as-welded and the post-ST-aged condition are shown in Figure 10 (c). The peak stress value, and as such the onset of necking, can be observed to commence outside of the weld bead region as defined in the model, thus in the parent material. This has produced the onset of necking outside of the weld bead region of the gauge length, whereas, for the model representing the solution heat-treated weld bead, the stress distribution is largely symmetric with the peak value predicted to be at the very centre of the gauge length. Importantly, the perfectly symmetrical, perfectly smooth edges of the gauge length in the FE model are a modelling simplification and limitation of the actual machined test piece. Consequently, any small machining mark, which would break the perfect symmetry and uniformity of the gauge length in a real experiment and as such naturally provide a nucleation point for the necking, is not represented in the FE model, which represents a 'perfect-world' test and does not fully capture the failure initiation occurring in a true tensile test.

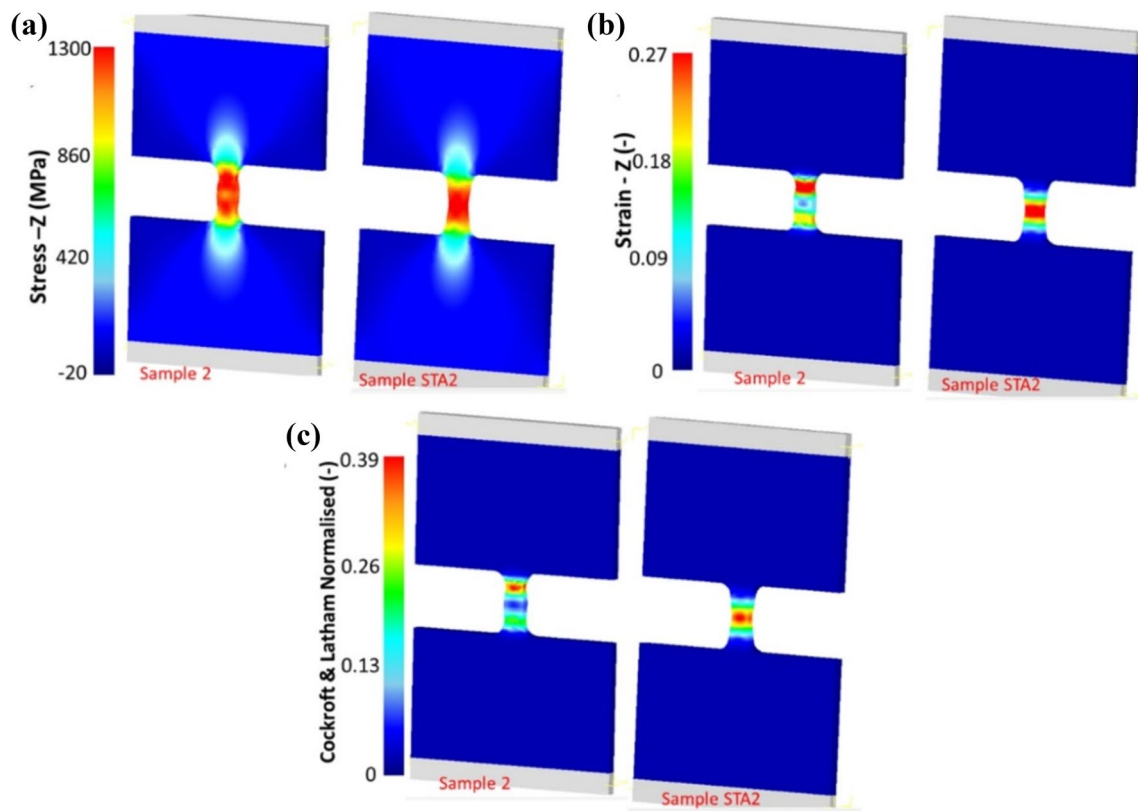


Figure 10 Simulation images showing **a** distribution of stress (σ_z) in (left) Sample 2 (as-welded) and (right) Sample STA2 (post-ST-aged); **b** distribution of strain (ϵ_z) in (left) Sample 2 and

(right) Sample STA2; **c** distribution of the normalised Cockroft and Latham damage parameter in (left) Sample 2; **b** and (right) Sample STA2.

However, predicting the likelihood for a sample to fracture by finite element methods is not purely a function of the multiple stress fields. The use of a reliable ductile fracture criteria implemented in the metal-forming software can help predict the potential likelihood for catastrophic failure and crack onset [24]. The Cockroft and Latham fracture criterion parameter is the most commonly used of these criteria. The normalised Cockroft and Latham fracture parameter was interrogated for the weld 2 tensile loading models. Gontarz and Piesiak [25] had previously simulated tensile testing of the Ti-6Al-4V alloy in dog-bone samples, and predicted a boundary fracture criterion of 0.354 for the alloy. As such, the normalised Cockroft and Latham fracture predictions within this experimental tensile specimen geometry illustrated probable locations for fracture to occur (Figure 10 (c)). These were largely matching the experiment (Figure 8), in a region just outside the weld bead region, still within the gauge length for the as-welded sample 2, and at the very centre of the weld bead and gauge length

for the solution-treated weld. By analysing the relevant model time-step based upon the ultimate tensile strength of the alloy, so an estimate for the critical value at catastrophic failure was slightly higher than the Gontarz prediction, around 0.38. However, it is likely that small-scale cracking and damage within this tensile specimen was suffered earlier, during the necking phase of the tensile sample.

Further comparison of the FE model predictions to the experimental data was conducted to interrogate the model for accuracy. The evolution of the peak strain (in the direction of tensile load) experienced within the FE model, from a node at the fracture location, was extracted and compared to the experimentally measured strain. Figure 11(a,b) illustrates how the strain evolution from FE model and experiment compare.

By considering the results from Fig. 11(a) for the as-welded test, FE predictions match reasonably for the first 100s, although the FE prediction then gradually diverges from experiment, underpredicting by

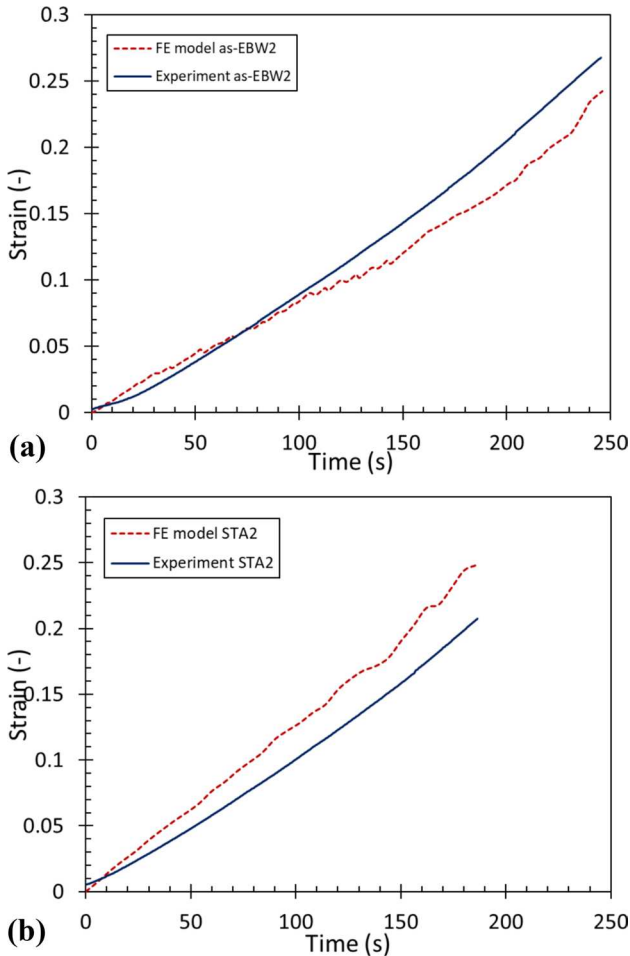


Figure 11 Evolution of the strain (ϵ_z) term during the FE simulation and during tensile experiment, for testing of a micro-tensile test piece taken from; **a** an as-welded weld line, and, **b** a solution treatment aged (STA) weld line.

approximately 0.03 strain at worst, an error of 11%. For the solution-treated aged (STA) test (fig. 11b), results were less accurate across all the duration of the tensile test, with FE this time overpredicting experimental strain, deviating from the experimental data immediately. Error was up to 0.05 strain, and a relative error of 21%. The over-prediction in one Ti64 condition while under-prediction in a different condition suggests uncertainty in the thermodynamic predictions for stress-strain curves. This may be as result of the simplifications inherent within the thermodynamics database computation to generate material data for subtly different condition of Ti64. There are also likely some re-meshing issues occasionally noted in the FE prediction, where the strain accumulation momentarily pauses.

Discussion

EBW Ti64 samples welded with two different energy densities (28 J/mm and 10 J/mm) were obtained through processing. The differing weld parameters, yielding different energy densities, both produced full penetration of the weld bead through the thickness of the plate, albeit with different weld bead dimensions and shapes. The higher energy density means a higher heat input per unit length of the weld path, which in particular due to the low thermal conductivity of titanium alloys leads to the larger weld pool size, as shown in Figure 4. More heat energy is transferred into the material per unit time, thus the width and depth of the weld pool, and the grain size within the fusion zone (FZ) increased (Table 3). The post-weld heat treatment only results in the reduction of HAZ size, and the weld pool depth and width remain nearly unchanged. However, the microstructural characteristics of the FZ greatly change after the PWHT. The heat treatments introduce higher elemental diffusion rate, which makes the welded material more homogeneous and thus there is less transition from BM to HAZ.

The microstructures within processed Ti64 samples are sensitive to the thermal condition during the manufacturing process and subsequent heat treatments. During the welding process, the thermal conditions lead to a weld with a transition microstructure from the FZ to the HAZ (Figures 5 and 7). Considerable martensitic α' phase is observed from the microscopy, embedded in the columnar β matrix in the FZ. The interlaced arrays of the acicular martensite formed the basketweave structure of martensite. The β columnar grains epitaxially grow towards the centre of the weld. During the EBW process, a very fast-cooling rate is induced. The acicular α' needles were formed from the prior β phase in a diffusionless, shear-type transformation process when the cooling rate is high (the critical range of 410–525°C/s) [26, 27]. The samples after PWHT have different microstructural variations because of heating, when compared with the as-welded samples. The martensitic α' phases coarsen in the FZ, secondary α phase precipitates in the HAZ and BM, and more equiaxed transformed β phases occurs in the BM. The martensitic phase is a supersaturated non-equilibrium phase which can be decomposed into the fine secondary α phase and β phase during the heat treatment. During the solution and ageing treatment, the diffusion of the alloying elements leads to α lath formation with transformed β phases (between the α laths).

Higher tensile properties were achieved in the welds compared with the base material. This indicates the electron beam welding is an effective technique to improve the joint efficiency. The microstructure of weld significantly affects the mechanical properties of the joint. The grain size and martensitic phase are both key factors controlling the performance. According to Equation 2, the finer grains can lead to lower local stress concentrations [28]. The ductility of the joint can be increased when deformation happens in more grains [29].

$$\sigma_p = Cd\sigma_a^2 \quad (2)$$

Where σ_p is stress concentration; C is a constant; d is grain size, and σ_a is external stress.

The sample with finer grains has higher strength due to Hall–Petch. Finer grains can not only reduce the dislocation slip velocity, but also obstruct the pile-up of dislocation. The large amount of martensitic phase with smaller space results in more interfaces in the structure, which can shorten the slip length. Moreover, the fine martensitic phases form a dislocation barrier and increase the tensile strength of the welds [8, 30, 31]. The mechanical property of welded samples enhances due to the kinetic hardening resulting from the mechanical contrast between the α and martensitic phases. The Al-depletion of martensitic phase is suspected to change the heterogeneous deformation substructure to a homogeneous deformation substructure, which leads to an increased ductility of martensitic phase [32]. Thus, the welded samples have increased ductility and strength. The strength loss of the welds after PWHT is due to the over-ageing of the martensite and the transformation to α and β . In addition, as the molten weld pool cooled down through the α and β region, the vanadium (V) content of the β phase increased and the martensite start (M_s) and martensite finish (M_f) temperature progressively decreased. It has been reported that M_s and M_f of Ti64 are 800°C and 630°C, respectively [33, 34]. Thus, it is likely that some retained β will be present in BM or metastable β phase in HAZ. During the post-weld heat treatments, β decomposes with the precipitation of fine α . This precipitation results in the harder HAZ and BM. Therefore, the FZ, HAZ and BM across the gauge length experienced the non-uniform deformation during the tensile test. The fracture of the STA samples occurred in the FZ, because the FZ is softer than

the other zones which underwent the larger localised strains.

Additionally, the full complex microstructural features that give rise to the resulting mechanical properties were not fully considered in the thermodynamic predictions of the alloy, thus the mechanical properties subsequently considered in FE were a simplification of the true metallurgical condition of the weld. However, the fact that the model was able to predict different locations for the fracture, inside the different zones of the simulated weld bead, suggests that the thermodynamic data within the framework is able to account for the primary strengthening mechanisms arising from the metallurgical phenomena within the weld and heat treatment processes.

Conclusion

The effects of post-weld heat treatments (PWHTs) on the microstructure and in situ tensile properties of electron beam welded (EBW) Ti64 welds were studied experimentally and with finite element (FE) simulation. The conclusions are shown as follows:

The post-weld heat treatments have negligible effect on the weld pool width and depth, but solely reduce the size of heat-affected zone (HAZ). This is because the microstructures are significantly affected after the heat treatment, but the fundamental thermo-physical properties of material are barely changed. After the PWHT, the microstructure significantly changed across the three different zones. The amount of fine needle-like martensitic phases can be observed in the fusion zone (FZ), which coarsens after the heat treatment. The ghost α phase decomposed into α and β lath phases in the heat-affected zone (HAZ). The presence of a fine interlamellar $\alpha+\beta$ structure within the transformed β grains can be observed in the base material (BM) of solution-treated & aged (STA) samples.

Electron beam welding can effectively improve the joint efficiency of Ti64. The maximum tensile strength is obtained in the as-welded samples and the minimum for the post-weld solid solution (STA) and ageing (A) samples.

Thermodynamic databases can predict yield strengths of the titanium alloy for different grain sizes, representing different post-weld heat treatment operations (PWHTs). Through FE modelling

using a single workpiece with different regions to represent different weld zones, the location for the likely necking and fracture can be predicted for the different heat-treated conditions in Ti64 alloy.

Acknowledgements

The authors wish to thank supporting staff at the School of Metallurgy and Materials, University of Birmingham, in particular Professor Yu-Lung Chiu, of the Centre for Electron Microscopy.

Data availability

FE modelling code input is available upon request to the corresponding authors via the supplied contact information.

Declarations

Conflicts of interest On behalf of all authors, the corresponding author states that there is no conflict of interest.

Ethical approval Ethical approval was granted for work contained within this manuscript.

Open Access This article is licensed under a Creative Commons Attribution 4.0 International License, which permits use, sharing, adaptation, distribution and reproduction in any medium or format, as long as you give appropriate credit to the original author(s) and the source, provide a link to the Creative Commons licence, and indicate if changes were made. The images or other third party material in this article are included in the article's Creative Commons licence, unless indicated otherwise in a credit line to the material. If material is not included in the article's Creative Commons licence and your intended use is not permitted by statutory regulation or exceeds the permitted use, you will need to obtain permission directly from the copyright holder. To view a copy of this licence, visit <http://creativecommons.org/licenses/by/4.0/>.

References

- [1] Banerjee D, Williams JC (2013) Perspectives on titanium science and technology. *Acta Mater* 61:844–879
- [2] Boyer RR (1996) An overview on the use of titanium in the aerospace industry. *Mater Sci Eng A* 213:103–114
- [3] C. Leyens, M. Peters, Titanium and titanium alloys: fundamentals and applications, John Wiley & Sons, Ltd, 2003.
- [4] Yunlian Q, Ju D, Quan H, Liying Z (2000) Electron beam welding, laser beam welding and gas tungsten arc welding of titanium sheet. *Mater Sci Eng* 280:177–181
- [5] Mohandas T, Banerjee D, Kutumba Rao VV (1998) Observations on impact toughness of electron beam welds of an $\alpha+\beta$ titanium alloy. *Mater Sci Eng A* 254(1–2):147–154
- [6] Sareesh N, Pillai MG, Mathew J (2007) Investigations into the effects of electron beam welding on thick Ti-6Al-4V titanium alloy. *J Mater Process Technol* 192:83–88
- [7] Meshram SD, Mohandas T (2010) A comparative evaluation of friction and electron beam welds of near- α titanium alloy. *Mater Des* 31:2245–2252
- [8] Kabir ASH, Cao X, Gholipour J, Wanjara P, Cuddy J, Birur A, Medraj M (2012) Effect of postweld heat treatment on microstructure, hardness, and tensile properties of laser-welded Ti-6Al-4V. *Metall Mater Trans A* 43:4171–4184
- [9] Tan LJ, Yao ZK, Wang T, Guo HZ (2011) Effect of post-weld heat treatment on microstructure and properties of electron beam welded joint of Ti2AlNb/TC11. *Mater Sci Technol* 27:1315–1320
- [10] W. Jia, H. Zhao, Y. Zan, P. Guo, X. Mao, (2018) Effect of heat treatment and laser shock peening on the microstructures and properties of electron beam welded Ti-6.5Al-1Mo-1V-2Zr joints, *Vacuum*. 155 496–503.
- [11] Liu H, Wang H, Zhang Z, Huang Z, Liu Y, Wang Q, Chen Q (2019) Enhancing the mechanical properties of electron beam welded TC17 titanium alloy joint by post-weld heat treatment. *J Alloys Compd* 810:151937
- [12] Tsai CJ, Wang LM (2014) Improved mechanical properties of Ti-6Al-4V alloy by electron beam welding process plus annealing treatments and its microstructural evolution. *Mater Des* 60:587–598
- [13] Lin HC, Wang LM (2011) Improved mechanical properties of Ti-15V-3Cr-3Sn-3Al alloy by electron beam welding process plus heat treatments and its microstructure evolution. *Mater Chem Phys* 126:891–897
- [14] Hayes BJ, Martin BW, Welk B, Kuhr SJ, Ales TK, Brice DA, Ghamarian I, Baker AH, Haden CV, Harlow DG, Fraser HL, Collins PC (2017) Predicting tensile properties of Ti-6Al-4V produced via directed energy deposition. *Acta Mater* 133:120–133

- [15] Mishurova T, Evsevlev S, Artzt K, Haubrich J, Sevostianov I, Requena G, Bruno G (2022) Micromechanical behavior of annealed Ti-6Al-4V produced by Laser Powder Bed Fusion. *European Journal of Materials* 2(1):186–201
- [16] Yang Q, Zhang P, Cheng L, Min Z, Chyu M, To AC (2016) Finite element modeling & validation of thermomechanical behavior of Ti-6Al-4V in directed energy deposition additive manufacturing. *Addit Manuf* 12:169–177
- [17] Ding J, Colegrove P, Mehnen J, Ganguly S, Sequeira Almeida PM, Wang F, Williams S (2011) Thermo-mechanical analysis of Wire and Arc Additive Layer Manufacturing process on large multi-layer parts. *Comp. Mat. Sci.* 50(12):3315–3322
- [18] Chiumenti M, Cevera M, Salmi A, Agelet de Saracibar C, Dialami N, Matsui K (2010) Finite element modeling of multi-pass welding and shaped metal deposition processes. *Comp. Methods. Appl. Mech. Eng.* 199:2243–2359
- [19] Lu Y, Turner R, Brooks J, Basoalto H (2022) A study of process-induced grain structures during steady state and non-steady state electron-beam welding of a titanium alloy. *J Mater Sci Tech* 113:117–127
- [20] Joun M, Choi I, Eom J, Lee M (2007) Finite element analysis of tensile testing with emphasis on necking. *Comp. Mater. Sci* 41(1):63–69
- [21] Saunders N, Guo Z, Li X, Miodownik AP, Schillé JP (2003) Using JMatPro to model materials properties and behavior. *JOM* 55:60–65
- [22] Z. Guo, N. Saunders, Modelling high temperature flow stress curves of titanium alloys, in: *MRS Int. Mater. Res. Conf.*, Chongqing, China, 2008: pp. 9–12.
- [23.] Lu Y, Turner R, Brooks J, Basoalto H (2021) Microstructural characteristics and computational investigation on electron beam welded Ti-6Al-4 V alloy. *J Mater Process Technol* 288:116837
- [24] Stebunov S, Vlasov A, Biba N (2018) Prediction of fracture in cold forging with modified Cockcroft-Latham criterion. *Procedia Manuf.* 15:519–526
- [25] A. Gontarz, J. Piesiak, Determining the normalized cockroft-Latham criterion for titanium alloy Ti6Al4V in tensile testing at room temperature, in: *Proc. World Congr. Mech. Chemical, Mater. Eng.*, Barcelona, Spain, 2015: pp. 4–7.
- [26.] Yang J, Yu H, Yin J, Gao M, Wang Z, Zeng X (2016) Formation and control of martensite in Ti-6Al-4V alloy produced by selective laser melting. *Mater Des* 108:308–318
- [27] Ahmed T, Rack HJ (1998) Phase transformations during cooling in $\alpha+\beta$ titanium alloys. *Mater Sci Eng A* 243:206–211
- [28] Kim YW (1995) Gamma titanium aluminide: their status and future. *JOM* 47:39–41
- [29] Chen G, Zhang B, Liu W, Feng J (2011) Crack formation and control upon the electron beam welding of TiAl-based alloys. *Intermetallics* 19:1857–1863
- [30] Kishore Babu N, S. Ganesh Sundara Raman, R. Mythili, S. Saroja, (2007) Correlation of microstructure with mechanical properties of TIG weldments of Ti-6Al-4V made with and without current pulsing. *Mater Charact* 58(7):581–587
- [31] Babu NK, Raman SGS, Murthy CVS, Reddy GM (2007) Effect of beam oscillation on fatigue life of Ti-6Al-4V electron beam weldments. *Mater Sci Eng A* 471:113–119
- [32] Dumas O, Malet L, Hary B, Prima F, Godet S (2021) Crystallography and reorientation mechanism upon deformation in the martensite of an $\alpha-\alpha'$ Ti-6Al-4V dual-phase microstructure exhibiting high work-hardening rate. *Acta Mater* 205:116530
- [33] Qazi JI, Senkov ON, Rahim J, Froes FH (2003) Kinetics of martensite decomposition in Ti-6Al-4V-xH alloys. *Mater Sci Eng A* 359:137–149
- [34] Tarín P, Gil FX, Ginebra MP, Manero JM, Prado JM, Solé M, Planell JA (1995) Structural Transformations in Ti-6Al-4V Alloy. *Le J. Phys. IV.* 5:317–322

Publisher's Note Springer Nature remains neutral with regard to jurisdictional claims in published maps and institutional affiliations.